



Design and Nonlinear Modeling of a Modular Cable-Driven Soft Robotic Arm

Xinda Qi , Graduate Student Member, IEEE, Yu Mei , Graduate Student Member, IEEE, Dong Chen, Member, IEEE, Zhaojian Li, Senior Member, IEEE, and Xiaobo Tan, Fellow, IEEE

Abstract—We propose a novel multisection cable-driven soft robotic arm inspired by octopus tentacles along with a new modeling approach. Each section of the modular manipulator is made of a soft tubing backbone, a soft silicone arm body, and two rigid endcaps, which connect adjacent sections and decouple the actuation cables of different sections. The soft robotic arm is made with casting after the rigid endcaps are 3D-printed, achieving low-cost and convenient fabrication. To capture the nonlinear effect of cables pushing into the soft silicone arm body, which results from the absence of intermediate rigid cable guides for higher compliance, an analytical static model is developed to describe the relationship between the bending curvature and the cable lengths. The proposed model shows superior prediction performance in experiments over that of a baseline model, especially under large bending conditions. Based on the nonlinear static model, a kinematic model of a multisection arm is further developed and used to derive a motion planning algorithm. Experiments show that the proposed soft arm has high flexibility and a large workspace, and the tracking errors under the algorithm based on the proposed modeling approach are up to 52% smaller than those with the algorithm derived from the baseline model.

Index Terms—Soft robotics, soft manipulators, cabledriven, kinematics modeling, statics modeling.

I. INTRODUCTION

OFT robotic manipulators have been widely proposed and developed for their various advantages, such as safe human—machine interactions, robustness, and flexibility [1], [2]. Compared with their fully rigid counterparts, soft manipulators can utilize the softness of their body structures to adapt to external

Manuscript received 11 January 2024; revised 26 March 2024 and 9 May 2024; accepted 15 May 2024. Date of publication 11 June 2024; date of current version 16 August 2024. This work was supported in part by the US National Institutes of Health under Grant 1UF1NS115817-01 and in part by National Science Foundation under Grant ECCS 2024649 and Grant CNS 2237577. Recommended by Technical Editor Li Zhang (AIM TE) and Senior Editor Qingze Zou (AIM SE). (Corresponding author: Xinda Qi.)

Xinda Qi, Yu Mei, Dong Chen, and Xiaobo Tan are with the Department of Electrical and Computer Engineering, Michigan State University, Lansing, MI 48824 USA (e-mail: qixinda@msu.edu; meiyu1@msu.edu; chendon9@msu.edu; xbtan@msu.edu).

Zhaojian Li is with the Department of Mechanical Engineering, Michigan State University, Lansing, MI 48824 USA (e-mail: lizhaoj1@msu.edu).

This article has supplementary material provided by the authors and color versions of one or more figures available at https://doi.org/10.1109/TMECH.2024.3402609.

Digital Object Identifier 10.1109/TMECH.2024.3402609

collisions and constraints and mitigate risks to humans, while being able to accomplish manipulation tasks [3], [4]. The advantages of soft manipulators make them competitive candidates for applications involving the handling of delicate and complex objects, as in fruit harvesting and medical surgeries [5], [6], [7].

Multiple structures and actuation methods have been developed for building soft robotics arms to achieve efficient deformation. For example, fluid-driven methods are widely used for soft actuators, where fluid pressures inside chambers are modulated to generate elastic deformation [8], [9], [10], [11]. Soft actuators have also been constructed with other mechanisms including smart materials [12]. In particular, the cable-driven method is popular thanks to its simplicity and high force-to-weight ratio [13], [14], where embedded eccentric cables driven by motors deliver torques to achieve deformation of the soft body.

To control the deformation of the soft arm effectively, models that capture the relationship between the actuation space and the task space of the robotic arm have been developed. The modeling is generally complex and often dependent on robot designs and actuation methods. Models for fluid-driven actuators are often built based on static and dynamic analysis [15]. For simple cabledriven actuators, models have been built based on geometry relationships [16]. Static models for tendon-driven manipulators have also been proposed to analyze the deformation of the elastic tendons [17]. In addition, models have been reported for the coupling and decoupling cable system of multisection soft manipulators [16], [18]. Piecewise constant curvature (PCC) models are widely utilized due to their simplicity [16], while other models, such as finite element method (FEM) models and Cosserat rod models are proposed with better accuracy but higher complexity [19], [20]. In addition, piecewise constant strain and geometric variable strain models have been proposed that allow more general settings [21].

Many biological structures and mechanisms have inspired the design of robotic systems, and conversely, the development of robots has provided bio-physical models for understanding biomechanics [22]. In this study, inspired by the longitudinal muscles in the octopus tentacles, we propose a novel decoupled modular cable-driven soft robotic arm fabricated with a integrated molding technique. We further develop a novel analytical static model that considers the prominent nonlinear effect of the cable pushing into the soft body of the robotic arm. To the best of the authors knowledge, this is the first effort in explicitly modeling the transverse deformation effect in soft cable-driven

1083-4435 © 2024 IEEE. Personal use is permitted, but republication/redistribution requires IEEE permission. See https://www.ieee.org/publications/rights/index.html for more information.

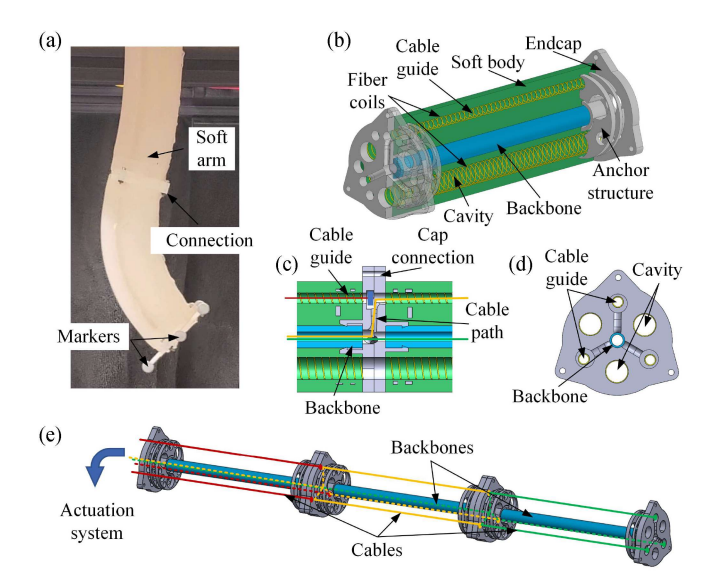


Fig. 1. Structures of the soft robotic arm. (a) Two-section modular soft robotic arm. (b) Structure for one section of the robotic arm. (c) Connection of two endcaps. (d) One endcap at the tip side of the section. (e) Cable paths for different sections of the soft robotic arm.

actuators, which extensively exists and potentially significantly influence the actuation length of the cable.

Specifically, a novel composite structure of a single section of the arm consists of multiple parts: flexible backbone, soft silicone body, multipurpose rigid caps, and embedded coil-reinforced cable guides with high compliance [see Fig. 1(b)]. A piece of soft tubing is selected as the backbone to constrain the axial deformation. Two rigid endcaps are attached to the ends of the backbone, which act as connectors between sections and anchor points for cables. The soft silicone body is made by casting with three specially-designed evenly embedded fiber-reinforced cable guides that protect the soft body while maintaining high compliance. Actuation cables in the cable guides provide contraction forces like longitudinal muscles while the cavities are able to reduce the bending stiffness of the soft arm.

The soft modular multisection robotic arm consists of identical sections with an embedded cable system. The unique actuation decoupling mechanism is achieved by the connection of the multipropose endcaps, which generate pathways between the cable guides and the backbone tubing [see Fig. 1(c) and (d)]. The actuation cables, with their one end fixed on the endcap, pass through the cable guides in one section and go into the backbone tubing through the pathways before they are attached to the corresponding driving motors, which presents a convenient routing scheme thank to the endcap design of the actuation decoupling mechanism [see Fig. 1(e)]. When one section of the arm has a bending deformation, its backbone maintains a nearly constant length, ensuring the lengths of the actuation cables for other sections do not passively change. During the bending motion of the multisection robotic arm, the backbone tubing protects the actuation system for other sections, separating the deformation of one section from the change of cable lengths of other sections, and thus achieving actuation decoupling between different sections of the robotic arm.

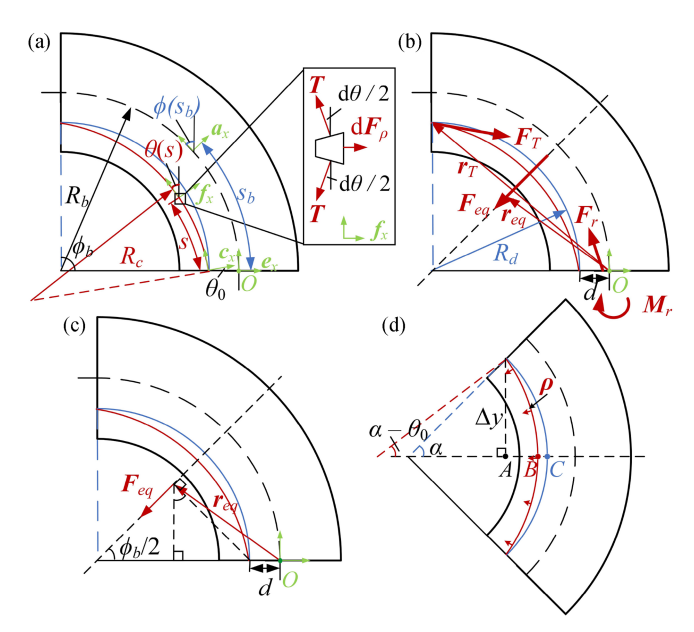


Fig. 2. Modeling of one section of the arm driven by a single cable. (a) Bending configuration for one section driven by a single cable. (b) External forces and moments applied by the cable to the soft section. (c) Total transverse force applied by the cable and its arm. (d) Actuation cable considering transverse deformation (red) and without transverse deformation (blue).

II. MATERIALS AND METHODS

Each section of the modular soft robotic arm was fabricated separately by using integrated molding and then assembled together. The endcaps and the molds for each section were fabricated with a 3-D printer (Objet Connex 350) using rigid material (Objet Vero White). After the molds were assembled with flexible tubing (Clear Masterkleer Soft PVC Plastic Tubing, McMaster-Carr), which acted as the backbone, a silicone material (Ecoflex 00-10, Smooth-On) was utilized to cast the soft body of each section, before different sections and the cable system were assembled. More details on the fabrication of the soft robotic arm and on the experimental setups are given in the Supplementary Material.

III. MODELING OF THE SOFT ROBOTIC ARM

The model for the multisection soft robotic arm is separated into two parts: A static model for a single section, which maps the actuation cable lengths to the bending configuration of one section and another model that characterizes the relationship between the bending configurations for all sections and the task space variables (in particular, the end position of the arm). A parameter list is provided in the Supplementary Material (S2) for the convenience of readers.

A. Static Model of a Section Driven by a Single Cable

The static model for a single section of the robotic arm is built based on the analysis of its bending deformation. Before studying a section with multiple actuation cables, we consider the case with a single actuating cable and analyze an arbitrary bending configuration [see Fig. 2(a)]. The cable and the support

of the section provide external forces. To simplify the static analysis, several assumptions are made as follows.

- A1) The backbone (dash line) of the soft section has a constant length.
- A2) The backbone and the cable (red line) have constant curvatures.
- A3) The backbone has bending deformations within one single plane.
- A4) The friction between the cables and the soft body of the arm is negligible.
- A5) The soft section of the arm has a linear bending stiffness with no hysteresis.
- A6) The cables have no slacks.

Refer to Fig. 2(a). Let s_b (subscript "b" for "backbone") be the arclength parameter for the backbone. The bending angle $\phi(s_b)$ of the section at a given point with an arclength s_b is defined as the angle of rotation between the two local frames at the base, $e = (e_x, e_y)$, and at the point with s_b on the backbone, $a = (a_x, a_y)$, and can be described as

$$\phi\left(s_{b}\right) = \frac{s_{b}}{R_{L}}\tag{1}$$

where R_b is the radius of the backbone curvature. The curvature of the backbone, κ_b , is written as: $\kappa_b = \frac{\mathrm{d}\phi}{\mathrm{d}s_b} = \frac{1}{R_b}$.

The curvature κ_c (subscript "c" for "cable") for the cable is

The curvature κ_c (subscript "c" for "cable") for the cable is described similarly: $\kappa_c = 1/R_c$, where R_c is the radius of the actuation cable curvature, and s is the arclength parameter for the cable. As illustrated in Fig. 2(a), $\theta(s)$ is the rotation angle between the base frame e and $f = (f_x, f_y)$, where f is the local frame at the point with an arclength of s on the cable.

Based on the force balance [see Fig. 2(a)], the transverse force density ρ between the cable and soft body [see Fig. 2(d)] is derived

$$\rho = \frac{\mathrm{d}F_{\rho}}{\mathrm{d}s} = T\kappa_c \tag{2}$$

where $\mathrm{d}F_{\rho}=T\mathrm{d}\theta$, d denotes the differential operator, T is the tension of the cable, F_{ρ} is the transverse force between the cable and the soft body, θ is used to denote $\theta(s)$ for simplicity, the notation "d" represents differential, and the relationship $\frac{\mathrm{d}\theta}{\mathrm{d}s}=\kappa_c$ is used in the derivation of (2).

Another assumption following the introduction of ρ is made to describe a simplified interaction model between the cable and the soft body of the arm.

A7) The maximum transverse deformation of the cable (|BC| in Fig. 2(d)) is proportional to the transverse force density ρ applied by the cable [see Fig. 2(d)].

Next, the transverse force density vector ρ^e at point s, viewed in the base frame e [see Fig. 2(a)], is calculated by using a rotation matrix R_f^e

$$\boldsymbol{\rho}^{\boldsymbol{e}}(\theta) = R_f^e \begin{bmatrix} -\rho \\ 0 \end{bmatrix} \tag{3}$$

$$R_f^e(\theta) = \begin{bmatrix} \cos \theta & -\sin \theta \\ \sin \theta & \cos \theta \end{bmatrix}. \tag{4}$$

The total transverse force F_{eq} (subscript "eq" for "equivalent total force") between the cable and the soft body [see Fig. 2(b)] can then be obtained by the following integration:

$$\boldsymbol{F}_{eq} = \int_0^l \boldsymbol{\rho}^e(\theta(s)) ds = T \begin{bmatrix} -\sin(\phi_b - \theta_0) + \sin\theta_0 \\ \cos(\phi_b - \theta_0) - \cos\theta_0 \end{bmatrix}$$
 (5)

where l is the cable length in the soft section, ϕ_b is the bending angle of the backbone at the tip, and θ_0 is the incident angle of the cable, which is the angle between the tangent line (c_y axis) of the cable at the base surface and the normal (e_y axis) of the base surface [see Fig. 2(a)].

The contraction force F_T applied by the cable tip to the soft section [see Fig. 2(b)] is calculated as

$$\boldsymbol{F}_{T} = R_{f}^{e} \left(\phi_{b} - \theta_{0} \right) \cdot \begin{bmatrix} 0 \\ -T \end{bmatrix} = T \begin{bmatrix} \sin \left(\phi_{b} - \theta_{0} \right) \\ -\cos \left(\phi_{b} - \theta_{0} \right) \end{bmatrix}. \quad (6)$$

From the force balance equation: $F_r + F_{eq} + F_T = 0$, where F_r (subscript "r" for "reaction") represents the support force applied by the base support of the soft section to the soft section [see Fig. 2(b)], one can derive

$$\boldsymbol{F}_{r} = -\boldsymbol{F}_{eq} - \boldsymbol{F}_{T} = T \begin{bmatrix} -\sin\theta_{0} \\ \cos\theta_{0} \end{bmatrix}. \tag{7}$$

Next, the moment balance of the section is analyzed with respect to the base point O [see Fig. 2(b)]. The arm r_T [see Fig. 2(b)] for F_T is derived as

$$\boldsymbol{r}_T = \begin{bmatrix} -d - 2R_d \sin^2(\phi_b/2) \\ 2R_d \sin(\phi_b/2) \cos(\phi_b/2) \end{bmatrix}$$
(8)

where R_d is the radius of the cable curvature [see Fig. 2(b)] when the transverse deformation of the cable is not considered, d is the distance between the incident point of the cable and the base point O of the section.

Since F_{eq} is located on the mirror-symmetric axis of the bending section [see Fig. 2(c)], the point of action of F_{eq} is irrelevant in computing the resulting moment around point O; in other words, the moment is the same regardless of the point of action of F_{eq} . We have thus chosen the point of action as illustrated in Fig. 2(c), with the associated arm vector

$$\boldsymbol{r}_{eq} = \begin{bmatrix} -d - R_d \sin^2(\phi_b/2) \\ R_d \sin(\phi_b/2) \cos(\phi_b/2) \end{bmatrix}.$$
 (9)

From the moment balance of the section: $M_r + M_{eq} + M_T = 0$, where M_r denotes the support moment [see Fig. 2(b)], M_{eq} and M_T are the moments generated by F_{eq} and F_T with respect to point O, respectively, [see Fig. 2(b)], and

$$\boldsymbol{M}_{eq} + \boldsymbol{M}_{T} = \boldsymbol{r}_{eq} \times \boldsymbol{F}_{eq} + \boldsymbol{r}_{T} \times \boldsymbol{F}_{T} = Td\cos\theta_{0} \quad (10)$$

one obtains

$$\boldsymbol{M}_r = -(\boldsymbol{M}_{eq} + \boldsymbol{M}_T) = -Td\cos\theta_0. \tag{11}$$

See the Supplemental Material (S2) for calculation details of this concise result. Next, the incident angle of the cable θ_0 [see

Fig. 2(a) and (d)] satisfies

$$\Delta y = (R_b - d)\sin\alpha = R_c\sin(\alpha - \theta_0) \tag{12}$$

which implies

$$\theta_0 = \alpha - \arcsin\left(\left(1 - \kappa_b d\right) \frac{\kappa_c}{\kappa_b} \sin \alpha\right)$$
 (13)

where $\alpha = \phi_b/2$.

Based on assumption (A7) and the geometric relationships [see Fig. 2(d)], one can obtain

$$\Delta h = |BC| = R_d(1 - \cos\alpha) - R_c(1 - \cos(\alpha - \theta_0)) \quad (14)$$

$$\rho = K_c \Delta h \tag{15}$$

where Δh is the maximum transverse deformation of the cable, and K_c is the coefficient in the simplified linear relationship between Δh and ρ , which is influenced by physical characters of the soft arm (e.g., elasticity modulus). The value of K_c is obtained via experimental calibration.

Based on assumption (A5), the relationship between the bending deformation and the external torque is derived by introducing a bending stiffness K_b

$$|M_{eq} + M_T| = |M_r| = M_r = K_b \kappa_b$$
 (16)

where $K_b \kappa_b$ is the internal elastic moment. The value K_b is also influenced by the physical characters of the arm and calibrated by using experiments.

Finally, by using the Equations (2), (11), (13)–(16), and the geometric relationships, the model for a single soft section driven by a single cable is captured by

$$\begin{cases}
K_b \kappa_b = T d \cos \theta_0 \\
\theta_0 = \alpha - \arcsin \left((1 - \kappa_b d) \frac{\kappa_c}{\kappa_b} \sin \alpha \right) \\
T = \frac{K_c}{\kappa_c} \left\{ \left(\frac{1}{\kappa_b} - d \right) (1 - \cos \alpha) - \frac{1}{\kappa_c} (1 - \cos (\alpha - \theta_0)) \right\} \\
l = R_c \left(\phi_b - 2\theta_0 \right) = \frac{1}{\kappa_c} \left(L \kappa_b - 2\theta_0 \right)
\end{cases}$$
(17)

where L is the length of the soft section's backbone. In the forward mapping from actuation to the robotic arm configuration, the backbone curvature κ_b is solved based on the cable length l by using a nonlinear equation set solver and numerical methods (e.g., "fsolve" in MATLAB), while in the inverse problem l is calculated based on a desired reference κ_b by using the nonlinear equation set solver. The incident angle θ_0 , cable curvature κ_c and cable tension T are intermediate variables, while d, L, K_c , and K_b are constants and ϕ_b and α are dependent on κ_b . The initial guess for the solution to the nonlinear equations is derived by solving the last three equations in (17) when we assume that there is no transverse deformation of the cable [blue curve in Fig. 2(a)]: $\theta_0 = 0$.

B. Static Model of a Section Driven by Multiple Cables

After the model for one section driven by one cable is obtained, the model for the case of a single section with multiple actuating cables is addressed, where we assume that there is no slack for any cable.

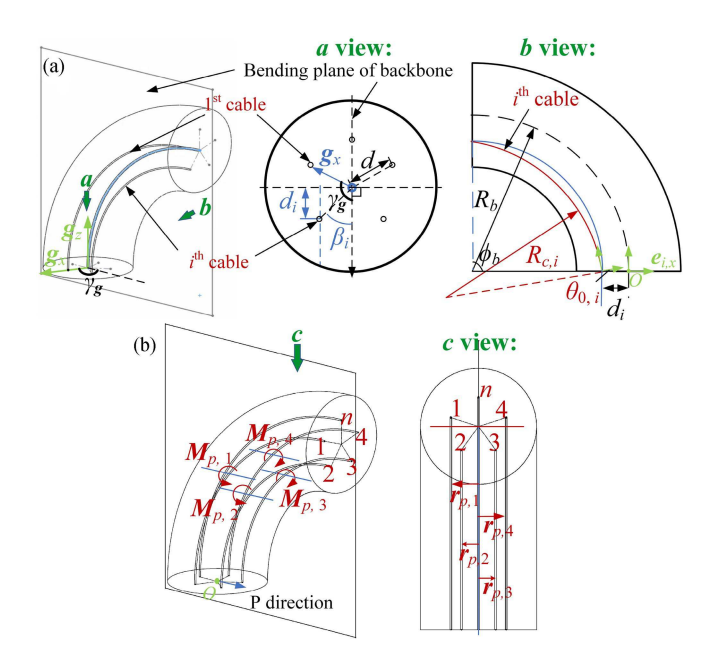


Fig. 3. Modeling of one section of the arm driven by multiple cables. (a) Bending configuration for one section of the arm driven by multiple cables. (b) External moments applied by multiple cables to the soft section in the P direction.

The bending configuration for the soft section with n evenly distributed cables (a general case) is defined by the bending angle ϕ_b and the bending orientation γ_g (γ_g is with respect to the base frame g) [see Fig. 3(a)]. A curved neutral surface is defined so that it is perpendicular to the bending plane and contains the backbone. The cables are indexed counterclockwise and the direction of the x-axis of the base frame g points to the first cable. The angle β_i between the ith cable orientation (in the base plane) and the bending direction is written as [see Fig. 3(a)]

$$\beta_i = \frac{2\pi(i-1)}{n} - \gamma_g \quad i = 1, 2, 3 \dots$$
 (18)

where n is the total number of the evenly distributed cables in the soft section.

The distance between the incident point of the *i*th cable and the neutral plane is calculated as

$$d_i = d\cos\beta_i \quad i = 1, 2, 3 \dots$$
 (19)

In the bending plane of the *i*th cable [see Fig. 3(a)], which is parallel to the bending plane of the backbone and contains the *i*th cable, the external force condition is analyzed as the single cable-driven case

$$\begin{cases}
\mathbf{F}_{r,i} = T_i \begin{bmatrix} -\sin\theta_{0,i} \\ \cos\theta_{0,i} \end{bmatrix} \\
|\mathbf{M}_{r,i}| = |-T_i d_i \cos\theta_{0,i}| \\
\theta_{0,i} = \alpha - \arcsin\left((1 - \kappa_b d_i) \frac{\kappa_{c,i}}{\kappa_b} \sin\alpha \right) \\
T_i = \frac{K_c}{\kappa_{c,i}} \left\{ \left(\frac{1}{\kappa_b} - d_i \right) (1 - \cos\alpha) - \frac{1}{\kappa_{c,i}} (1 - \cos(\alpha - \theta_{0,i})) \right\}
\end{cases} (20)$$

where T_i , $\theta_{0,i}$, and $\kappa_{c,i}$ are the cable tension, incident angle, and curvature of the *i*th cable, respectively, and $F_{r,i}$ and $M_{r,i}$ are

the support force and moment components induced by the *i*th cable, respectively, in local frame e_i [see Fig. 3(a)].

Then, one can calculate the total bending moment applied by the cables for the section

$$|\mathbf{M}| = \left| \sum_{i=1}^{n} -\mathbf{M}_{r,i} \right| = K_b \kappa_b. \tag{21}$$

Furthermore, since there is no bending deformation in the direction perpendicular to the bending direction, and based on assumption (A3), the total external moment applied by cables in the P direction with respect to O [see Fig. 3(b)] is zero

$$\sum_{i=1}^{n} M_{p,i} = 0 (22)$$

where $M_{p,i}$ is the external moment applied by the *i*th cable with respect to O, in the P direction [see Fig. 3(b)].

The arm $r_{p,i}$ of the external forces for $M_{p,i}$ is the distance between the bending plane of the *i*th cable and the bending plane of the backbone [see Fig. 3(b)], whose direction is perpendicular to the bending plane with the magnitude

$$r_{p,i} = d\sin\beta_i. \tag{23}$$

Thus, the lateral moment $\boldsymbol{M}_{p,i}$ applied by the ith cable is derived as

$$M_{p,i} = \mathbf{F}_{T,i,y} \times \mathbf{r}_{p,i} + \int_0^{l_i} \boldsymbol{\rho}_{i,y}^e(s) \times \mathbf{r}_{p,i} ds$$

= $-\mathbf{F}_{r,i,y} \times \mathbf{r}_{p,i}$ (24)

where $F_{T,i,y}$, $\rho_{i,y}^e$, and $F_{r,i,y}$ are the components along $e_{i,y}$ axis (or \mathbf{g}_z axis) of the $F_{T,i}$, ρ_i^e , and $F_{r,i}$, respectively.

Then, based on (19)–(24) and the geometric relationships, the kinematic model for a soft section of the arm actuated by multiple cables is derived as

$$\begin{cases}
\sum_{i=1}^{n} T_i d \cos \theta_{0,i} \cos \beta_i = K_b \kappa_b \\
\sum_{i=1}^{n} T_i d \cos \theta_{0,i} \sin \beta_i = 0 \\
\theta_{0,i} = \alpha - \arcsin\left(\left(1 - \kappa_b d_i\right) \frac{\kappa_{c,i}}{\kappa_b} \sin \alpha\right) \\
T_i = \frac{K_c}{\kappa_{c,i}} \left\{ \left(\frac{1}{\kappa_b} - d_i\right) \left(1 - \cos \alpha\right) - \frac{1}{\kappa_{c,i}} \left(1 - \cos(\alpha - \theta_{0,i})\right) \right\} \\
l_i = R_{c,i} \left(\phi_b - 2\theta_{0,i}\right) = \frac{1}{\kappa_{c,i}} \left(L\kappa_b - 2\theta_{0,i}\right).
\end{cases}$$
(25)

In the forward mapping from actuation to arm configuration, given the cable lengths l_i , the backbone curvature κ_b and the bending orientation γ_g [manifested via β_i in (18)] are obtained by solving the (25). $\theta_{0,i}, \kappa_{c,i}$, and T_i are intermediate variables, d, L, K_c , and K_b are constants, and ϕ_b , α are fully determined by κ_b . Therefore, in the forward mapping problem, there are (3n+2) unknowns and (3n+2) independent equations. In the inverse mapping problem, the lengths l_i for different cables are calculated based on the desired reference values of κ_b and γ_g by solving the same (25). It is noticed that n (the number of the cables) is required to be larger than 2 to achieve a redundant actuation system for all of the bending orientations considering the limitation that T_i is nonnegative (in the inverse mapping, considering the (25), substituting β_i by using γ_g , the numbers of

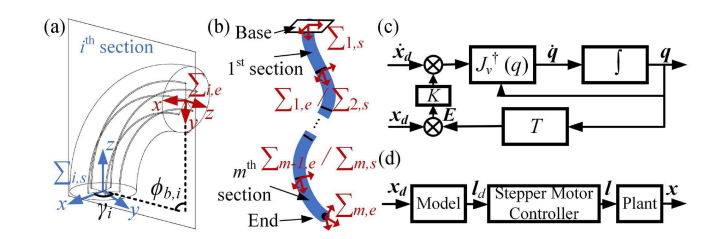


Fig. 4. Modeling of a multisection soft robotic arm. (a) Variables of bending configuration for one section. (b) Local frames for different sections. (c) Inverse kinematics solver for the bending configurations of different sections based on the reference of the end position. (d) Open loop control of the soft robotic arm based on the proposed model. \boldsymbol{x} and \boldsymbol{t} are the end position of the soft robotic arm and the actuation cable lengths, respectively, for which \boldsymbol{x}_d and \boldsymbol{t}_d are the corresponding target values.

independent equations and the unknown variables are (3n + 2) and (4n), respectively). The initial guess of the nonlinear system is obtained by solving the last three rows in (25), where we assume that there is no transverse deformation of the cables: $\theta_{0,i} = 0$.

C. Modeling of a Multisection Soft Arm

For the multisection soft robotic arm, the kinematic model between the task space configuration (in particular, the end position) and the bending configuration for each section is built by using homogeneous transformation matrices [16]. Specifically, considering the thickness of the rigid endcaps, one can divide each section of the arm into three parts: straight, bending, and straight. The transformation matrix $T_{i,e}^{i,s}$, which transforms vectors in the end frame $\Sigma_{i,e}$ to those in the base frame $\Sigma_{i,s}$ for the *i*th section [see Fig. 4(a)], is given by

$$T_{i,e}^{i,s} = \begin{bmatrix} I & \mathbf{p}_{0,i} \\ 0 & 1 \end{bmatrix} \begin{bmatrix} R_z (\gamma_i) & 0 \\ 0 & 1 \end{bmatrix} \begin{bmatrix} R_y (\phi_{b,i}) & \mathbf{p}_i \\ 0 & 1 \end{bmatrix}$$
$$\cdot \begin{bmatrix} R_z (-\gamma_i) & 0 \\ 0 & 1 \end{bmatrix} \begin{bmatrix} I & \mathbf{p}_{0,i} \\ 0 & 1 \end{bmatrix}$$
(26)

where $\phi_{b,i}$ and γ_i (γ_i is with respect to a general base frame $\Sigma_{i,s}$ that is not dependent on the cable distribution) are the bending angle and orientation for the ith section, respectively, $p_i = \begin{bmatrix} (1-\cos\phi_{b,i})/\kappa_{b,i} & 0 & \sin\phi_{b,i}/\kappa_{b,i} \end{bmatrix}^T$ is the in-plane displacement from the base to tip for the ith section, $\kappa_{b,i}$ is the curvature of the backbone of the ith section, $p_{0,i} = \begin{bmatrix} 0 & 0 & h \end{bmatrix}^T$ is the displacement of the straight part and h is the thickness of the endcaps. I is a 3-D identity matrix, $R_z(\gamma_i)$, $R_y(\phi_{b,i})$, and $R_z(-\gamma_i)$ are the 3-D rotation matrices around the z-, y-, and z-axes for the angle γ_i , $\phi_{b,i}$, and $-\gamma_i$, respectively.

z-axes for the angle γ_i , $\phi_{b,i}$, and $-\gamma_i$, respectively. The transformation matrix $T_{m,e}^{1,s}$, which transforms vectors in the end frame $\Sigma_{m,e}$ to those in the base frame $\Sigma_{1,s}$ of the m-section arm, and the end position of the arm $p_t^{1,s}$ (subscript "t" for "tip") in $\Sigma_{1,s}$ [see Fig. 4(b)] can be calculated as

$$T_{m,e}^{1,s} = \prod_{i=1}^{m} T_{i,e}^{i,s}$$
 (27)

$$\boldsymbol{p}_{t}^{1,s} = T_{m,e}^{1,s} \cdot \boldsymbol{p}_{t}^{m,e} \tag{28}$$

where
$$\boldsymbol{p}_{t}^{m,e} = \begin{bmatrix} 0 & 0 & 0 & 1 \end{bmatrix}^{T}$$
.

For the inverse kinematics [23], the linear velocity Jacobian matrix J_v for the end position of the *m*-section arm with respect to the variables of bending configuration of each section is calculated as

$$J_v = J_{\boldsymbol{p}_t^{1,s}}(\boldsymbol{q}) = \begin{bmatrix} \frac{\partial \boldsymbol{p}_t^{1,s}}{\partial q_1} & \dots & \frac{\partial \boldsymbol{p}_t^{1,s}}{\partial q_{2m}} \end{bmatrix}$$
(29)

where $\mathbf{q} = \begin{bmatrix} \gamma_1 & \kappa_{b,1} & \dots & \gamma_m & \kappa_{b,m} \end{bmatrix}^T$ is the set of variables of the bending configurations of all sections. The calculated J_v is omitted for brevity and a small value δ_κ is added to $\kappa_{b,i}$ when $\kappa_{b,i} \to 0$ for numerical stability. At least two sections are required for the arm to provide redundancy for tracking desired end positions in 3-D space.

Once J_v is obtained, one can use the following method to approach the configurations given the desired task space output (inverse kinematics) by using the Levenberg–Marquardt method [24]

$$\dot{\boldsymbol{q}} = J_v^{\dagger} \mathcal{V} + \left(I - J_v^{\dagger} J_v \right) \dot{\boldsymbol{q}}_0 \tag{30}$$

where $J_v^{\dagger} = J_v^T (J_v J_v^T + k^2 I)^{-1}$ is the pseudoinverse of J_v , I is an identity matrix, k is a small positive number, $\mathcal{V} = \dot{\boldsymbol{x}}_d(t)$ is the velocity vector of the tracking trajectory $\boldsymbol{x}_d(t)$ (subscript "d" for "desired"), $\dot{\boldsymbol{q}}_0$ is any vector with the shape of $\dot{\boldsymbol{q}}$ and set to zero for the minimum energy criterium.

By using the Euler method [25] to integrate the velocities, the references for the bending configuration variables are calculated

$$\mathbf{q}\left(t_{k+1}\right) = \mathbf{q}\left(t_{k}\right) + J_{v}^{\dagger}\left(\mathbf{q}\left(t_{k}\right)\right) \cdot \dot{\mathbf{x}}_{d}\left(t_{k}\right) \cdot \Delta t \tag{31}$$

where $q(t_k)$ and $q(t_{k+1})$ denote q at the time steps t_k and t_{k+1} , respectively.

Closed-loop feedback is further implemented in the solver [see Fig. 4(c)] to reduce the error accumulated by the numerical integration with (31)

$$\dot{\boldsymbol{q}} = J_v^{\dagger}(\boldsymbol{q}) \left(\dot{\boldsymbol{x}}_d + K \cdot \boldsymbol{E} \right) \tag{32}$$

where $\boldsymbol{E} = \boldsymbol{x}_d - T_{m,e}^{1,s}(\boldsymbol{q}) \cdot \boldsymbol{p}_t^{m,e}$ is the feedback error and K is a positive diagonal gain matrix. Once \boldsymbol{q} is obtained, we can use the (25) to calculate the cable lengths l_i for different actuation cables for all sections. Thus, by combining the kinematic model for a multisection arm and the static model for single section, an analytical model can be built for handling the modeling of a soft arm with an arbitrary number of sections.

IV. RESULTS

A. Baseline Model for the Soft Robotic Arm

Extensive experiments have been conducted to validate the proposed model. For a fair comparison, a static baseline model was built based on the same assumptions (including the PCC assumption), except the consideration of the transverse deformation induced by the cables. The multisection part of the baseline model was kept the same as that of the proposed model. In this way, the influence of considering the transverse

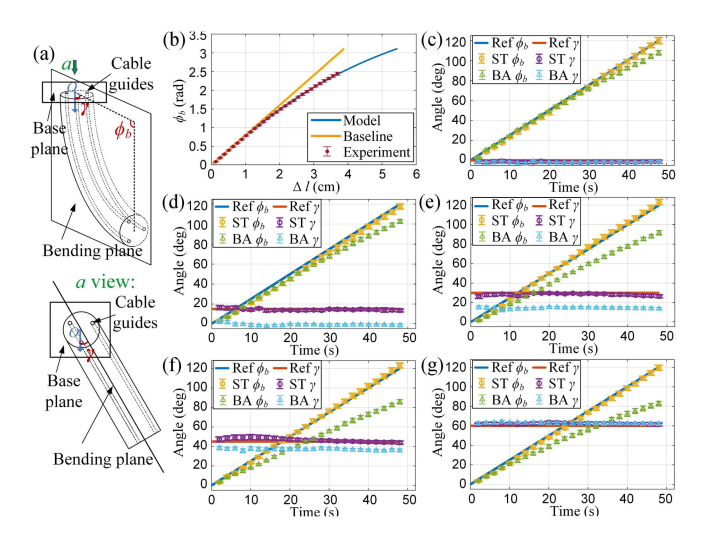


Fig. 5. Experiment results for a single section of the soft robotic arm. (a) Bending configuration of one section in experiments. (b) Relationship between cable contraction $\Delta l=L-l$ and bending angle ϕ_b with single cable actuation, comparing the predictions of the proposed model and the baseline model with the experimental data. (c) Tracking different bending angle ϕ_b when $\gamma=0^\circ$ using the baseline model (BA) and the proposed model (ST). (d) Tracking different ϕ_b when $\gamma=15^\circ$. (e) Tracking different ϕ_b when $\gamma=30^\circ$. (f) Tracking different ϕ_b when $\gamma=45^\circ$. (g) Tracking different ϕ_b when $\gamma=60^\circ$. The error bars denote the standard deviations of three runs for each bending configuration in the results.

deformation can be isolated from those of other factors. Note that the proposed model reduces to the baseline model once the transverse deformation effect is ignored (assigning $\theta_{0,i}=0$). The derived baseline model shares the same form as in the existing literature [16], where the curvature $\kappa_{c,i}$ and the length l_i of the *i*th cable in a section [blue curve in Fig. 3(a)] are derived as

$$\frac{1}{\kappa_b} = \frac{1}{\kappa_{c,i}} + d_i \tag{33}$$

$$l_i = R_{c,i} \cdot \phi_b = \frac{\kappa_b}{\kappa_{c,i}} L \tag{34}$$

where d_i is derived from (19), κ_b and L are the curvature and the length of the backbone, respectively.

B. Parameter Identification

The geometric parameters including (L,d) were measured directly from the prototype. The total length of the two-section arm was 206 mm and the diameter of the soft arm D was 28 mm. The bending stiffness K_b for a single soft section was calculated by using (11) and (16) assuming $\theta_0 \approx 0$ when ϕ_b was small, where T and ϕ_b were measured by a force sensor and a motion capture system when a single section was driven by one cable, respectively.

The relationship between a single cable contraction length Δl and ϕ_b [see Fig. 5(b)] was obtained in experiments for one soft section driven by a single cable, where the experimental results [see Fig. 5(b)] were used to identify K_c by using (17). The experimental results and the estimations of the bending deformation of one section driven by one cable based on the baseline model and the proposed model [see (17)] with the identified parameters

are shown in Fig. 4(b). The experimental setups for identifying K_b and K_c , the measured geometry parameters, and identified parameters (L, d, K_b, K_c) are elaborated in the Supplementary Material (S3).

C. Experimental Results for a Single Section

The single cable actuation results [see Fig. 5(b)] showed that, compared with the baseline model, the proposed static model was better in describing the nonlinear relationship between the cable actuation and the bending angle for the soft robotic arm, especially when the bending angle was relatively large. The simulation results of the proposed model and the real experiment data showed good agreements [see Fig. 5(b)], validating the prediction accuracy of the model. The results also indicated that the proposed model maintained high accuracy when the transverse deformation induced by the cable became more significant. The prediction by the baseline model, on the other hand, became worse when such effects became non-negligible under stronger actuation. After the model parameters were identified, extensive experiments were conducted to compare the accuracy of the baseline model and the proposed model [see (25)], where an open loop control without feedback was used [see Fig. 4(d)]. A single section of the arm was used to track different bending angles ϕ_b in specific bending orientations γ by using different models [see Fig. 5(a)]. The experimental setups, strategy for multicable redundancy, data processing methods for the results, and the high computation efficiency of the models (taking less than 1 ms to solve in MATLAB) are elaborated in Supplementary Material (S3).

The experiment results of the bending configurations (ϕ_b, γ) of the single section arm controlled by multiple cables by using different models are shown in Fig. 5(c)–(g). In the experiments, it was shown that the tracking accuracy of the proposed static model was significantly better than the baseline model in the experimental range [see Fig. 5(c)–(g)], indicating the importance and effectiveness of considering the transverse deformation of the cable in the proposed robotic arm. In particular, the tracking errors in ϕ_b and γ for the proposed model were small for different bending configurations. In comparison, the tracking error in ϕ_b for the baseline model increased together with the target ϕ_b when the target γ was fixed, while the tracking error in γ for the baseline model was almost constant and was considerable in some cases despite the changing of the target ϕ_b when the target γ was fixed.

Moreover, it was also shown that in the experiment range, the tracking error in ϕ_b for the baseline model increased with larger target γ when the target ϕ_b was fixed. The maximum ϕ_b tracking error increased from about 12° to about 37° when the target γ increased from 0° to 60° , respectively. The γ tracking error for the baseline model increased from about 0° to 16° when the target γ increased from 0° to 30° , respectively, and then decreased to near 0 when the target γ increased to 60° . It was noticed that for both models, the γ tracking error approached 0 when target γ was 0° and 60° , which was attributed to a single effective cable contraction and two effective cable contractions with the same contraction length, respectively. Specifically, when the

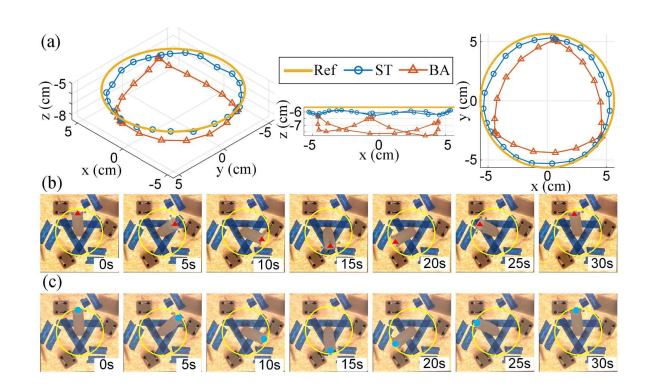


Fig. 6. Experiment results for a single section of the soft robotic arm tracking a circular trajectory. (a) Trajectories of the end position of the single section by using the baseline model (BA) and the proposed model (ST). (b) Illustration of movement and bending of the single section by using BA. (c) Illustration of movement and bending of the single section by using ST. In (b) and (c), yellow curves indicate the reference trajectory and red/blue dots indicate the tip of the arm.

target γ was 0, there was only one effective actuation cable (the other two cable were almost slack) for both the baseline model and the proposed model, and the bending orientation γ in the experiment naturally stayed around 0, which was the same as the orientation of the actuation cable. When the target γ was 60° , the two actuation cables shared the same contraction length (the third cable was almost slack) for both the baseline model and proposed model, and γ in the experiment stayed near 60° because of the actuation and structure symmetry.

A trajectory tracking experiment for the end of the single section was further conducted where the trajectory reference was included in its workspace. The experiment showed that the average tracking error of the single section (1.58 cm) by using the proposed model [see (25)] was about 35% smaller than that (2.43 cm) of the baseline model [see Fig. 6(a)]validating the effectiveness of the proposed model, and the soft section had flexible and versatile bending configurations [see Fig. 6(b) and (c)]. A video of these experiments and those in Section IV-D can be viewed online¹ (see the video in the Supplementary Material).

D. Experimental Results for a Two-Section Soft Robotic Arm

A multisection arm was assembled and utilized for the comparison of the baseline model and the proposed model, and its performance was further evaluated. For simplicity, a two-section arm was assembled and controlled to track a circular trajectory within its workspace by using the baseline model and the proposed model. The experiment results showed that, the average tracking error with the proposed model (3.76 cm) was about 36% smaller compared with the baseline model (5.92 cm), and the trajectory achieved with the open loop controller based on the proposed model was closer to the reference [see Fig. 7(a)–(c); also see the Supplementary Video]. The tracking error of the two-section soft arm was larger compared with that with a single section, which might be attributed to the error

¹[Online]. Available: https://youtu.be/I-e1PxHwG1Y

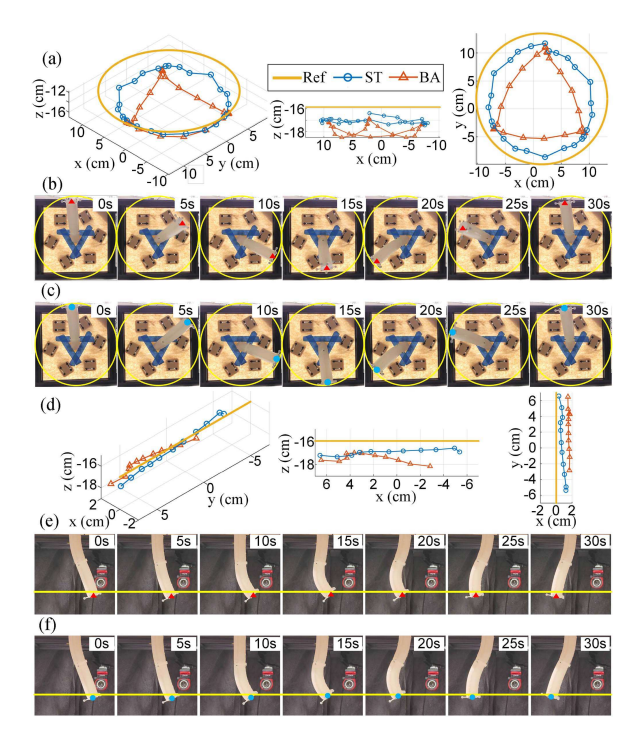


Fig. 7. Experiment results for a two-section soft robotic arm. (a) Trajectories of the end position of the arm tracking a circular path by using the baseline model (BA) and the proposed static model (ST). (b) Illustration of movement and bending of the arm tracking a circular path by using BA. (c) Illustration of movement and bending of the arm tracking a circular path by using ST. (d) Trajectories of the end position of the arm tracking a straight path by using BA and ST. (e) Illustration of movement and bending of the arm tracking a straight path by using BA. (f) Illustration of movement and bending of the arm tracking a straight path by using ST. In (b), (c), (e), and (f), yellow curves indicate the reference trajectory and red/blue dots indicate the tip of the arm.

accumulation between multiple sections and a more prominent gravity influence for the base section of the arm.

In addition, the two-section arm was controlled to track a straight trajectory within its workspace by using the models, where the average tracking error (1.70 cm) of the proposed model was about 52% smaller than that of the baseline model (3.52 cm) [see Fig. 7(d)–(f)] showing the advantage of the proposed model. Besides the comparison between the proposed model and the baseline model, by evaluating a normalize tracking error (the ratio of the static tracking error in open-loop control over the total arm length), it was found that the tracking error based on the proposed model (about 18.3%, 8.3% in circular, straight tests, respectively) was comparable to that based on a state-of-art FEM modeling approach (about 12.5%) in [19], while the proposed model was much more computationally efficient (see S3 in the Supplementary Material).

In summary, the extensive experiments showed the advantage of the proposed static model as compared to a baseline model and validated the flexibility and dexterity of the proposed soft robotic arm.

V. CONCLUSION

In this article, we designed an octopus-inspired soft robotic arm and developed a novel kinematic model to characterize its flexible movements. The modular design of the soft arm enabled longer arm prototypes and permitted a decoupling cable actuation system for different sections that simplified the modeling. The hybrid fabrication method of 3-D printing and casting resulted in low-cost and easy-to-build prototypes. An analytical static model was built to capture the transverse deformation of the cable during actuation, which was largely ignored in the literature.

Extensive experiments were conducted to validate the proposed model and the static baseline model was used for a fair comparison. The modeling accuracy was evaluated in the cable actuation experiments [see Fig. 5(b)] and tracking experiments (see Figs. 5–7). The results of tracking experiments for a single section of the soft arm showed an evident advantage and smaller tracking errors for the proposed model over the baseline model in terms of bending angle, orientation, and the end position of the arm. Experiments with a two-section arm further supported the efficiency of the proposed model in tracking circular and straight trajectories for the endpoint and demonstrated the dexterity of the proposed soft arm.

We note that our modeling approach was not only motivated by and particularly relevant to the proposed modular cabledriven soft robotic arm, but also applicable to many other cabledriven robotic arms, especially those not using rigid spacers, examples of which are abundant [26], [27]. Even for the soft arms with multiple rigid spacers, the transverse deformation phenomenon would still exist in the areas where the cables and the soft body interact directly.

For future work, first, we plan to relax the current geometric assumption (PCC assumption) for the soft arm by considering the moments generated by the gravity and external forces, using an iterative approach similar to that in Fairchild et al. [28]. We will also explore the related dynamic model with external interactions. Finally, we will develop integrated embedded sensors (e.g., soft strain sensors) for the soft robotic arm, so that real-time bending configuration data for the arm are made available for feedback control.

REFERENCES

- Z. Xie et al., "Octopus arm-inspired tapered soft actuators with suckers for improved grasping," Soft Robot., vol. 7, no. 5, pp. 639–648, 2020.
- [2] P. Palmieri, M. Melchiorre, and S. Mauro, "Design of a lightweight and deployable soft robotic arm," *Robotics*, vol. 11, no. 5, 2022, Art. no. 88.
- [3] X. Liang, H. Cheong, Y. Sun, J. Guo, C. K. Chui, and C.-H. Yeow, "Design, characterization, and implementation of a two-DOF fabric-based soft robotic arm," *IEEE Robot. Autom. Lett.*, vol. 3, no. 3, pp. 2702–2709, Jul. 2018
- [4] X. Wang, H. Kang, H. Zhou, W. Au, M. Y. Wang, and C. Chen, "Development and evaluation of a robust soft robotic gripper for apple harvesting," *Comput. Electron. Agriculture*, vol. 204, 2023, Art. no. 107552.
- [5] M. Cianchetti, T. Ranzani, G. Gerboni, I. De Falco, C. Laschi, and A. Menciassi, "Stiff-flop surgical manipulator: Mechanical design and experimental characterization of the single module," in *Proc. IEEE/RSJ Int. Conf. Intell. Robots Syst.*, 2013, pp. 3576–3581.
- [6] A. Diodato et al., "Soft robotic manipulator for improving dexterity in minimally invasive surgery," Surg. Innov., vol. 25, no. 1, pp. 69–76, 2018.
- [7] Z. Wang, S. Hirai, and S. Kawamura, "Challenges and opportunities in robotic food handling: A review," *Front. Robot. AI*, vol. 8, 2022, Art. no. 789107.
- [8] X. Chen, X. Zhang, Y. Huang, L. Cao, and J. Liu, "A review of soft manipulator research, applications, and opportunities," *J. Field Robot.*, vol. 39, no. 3, pp. 281–311, 2022.

- [9] R. K. Katzschmann, C. Della Santina, Y. Toshimitsu, A. Bicchi, and D. Rus, "Dynamic motion control of multi-segment soft robots using piecewise constant curvature matched with an augmented rigid body model," in *Proc.* 2nd IEEE Int. Conf. Soft Robot., 2019, pp. 454–461.
- [10] X. Qi, H. Shi, T. Pinto, and X. Tan, "A novel pneumatic soft snake robot using traveling-wave locomotion in constrained environments," *IEEE Robot. Autom. Letters*, vol. 5, no. 2, pp. 1610–1617, 2020.
- [11] X. Qi, T. Gao, and X. Tan, "Bioinspired 3d-printed snakeskins enable effective serpentine locomotion of a soft robotic snake," *Soft Robot.*, vol. 10, no. 3, pp. 568–579, 2023.
- [12] Z. Xing, J. Zhang, D. McCoul, Y. Cui, L. Sun, and J. Zhao, "A super-lightweight and soft manipulator driven by dielectric elastomers," *Soft Robot.*, vol. 7, no. 4, pp. 512–520, 2020.
- [13] C. Li and C. D. Rahn, "Design of continuous backbone, cable-driven robots," J. Mech. Des., vol. 124, no. 2, pp. 265–271, 2002.
- [14] J. Lai, K. Huang, B. Lu, Q. Zhao, and H. K. Chu, "Verticalized-tip trajectory tracking of a 3D-printable soft continuum robot: Enabling surgical blood suction automation," *IEEE/ASME Trans. Mechatronics*, vol. 27, no. 3, pp. 1545–1556, Jun. 2022.
- [15] Y. Mei, P. Fairchild, V. Srivastava, C. Cao, and X. Tan, "Simultaneous motion and stiffness control for soft pneumatic manipulators based on a lagrangian-based dynamic model," in *Proc. Amer. Control Conf.*, 2023, pp. 145–152.
- [16] R. J. Webster III and B. A. Jones, "Design and kinematic modeling of constant curvature continuum robots: A review," *Int. J. Robot. Res.*, vol. 29, no. 13, pp. 1661–1683, 2010.
- [17] D. B. Camarillo, C. F. Milne, C. R. Carlson, M. R. Zinn, and J. K. Salisbury, "Mechanics modeling of tendon-driven continuum manipulators," *IEEE Trans. Robot.*, vol. 24, no. 6, pp. 1262–1273, Dec. 2008.
- [18] F. Renda, M. Giorelli, M. Calisti, M. Cianchetti, and C. Laschi, "Dynamic model of a multibending soft robot arm driven by cables," *IEEE Trans. Robot.*, vol. 30, no. 5, pp. 1109–1122, Oct. 2014.

- [19] T. Morales Bieze, A. Kruszewski, B. Carrez, and C. Duriez, "Design, implementation, and control of a deformable manipulator robot based on a compliant spine," *Int. J. Robot. Res.*, vol. 39, no. 14, pp. 1604–1619, 2020.
- [20] D. Trivedi, A. Lotfi, and C. D. Rahn, "Geometrically exact models for soft robotic manipulators," *IEEE Trans. Robot.*, vol. 24, no. 4, pp. 773–780, Aug. 2008.
- [21] F. Renda, C. Armanini, A. Mathew, and F. Boyer, "Geometrically-exact inverse kinematic control of soft manipulators with general threadlike actuators' routing," *IEEE Robot. Autom. Lett.*, vol. 7, no. 3, pp. 7311–7318, Jul. 2022.
- [22] Y. Wu et al., "Insect-scale fast moving and ultrarobust soft robot," Sci. Robot., vol. 4, no. 32, 2019, Art. no. eaax1594.
- [23] L. Sciavicco and B. Siciliano, Modelling and Control of Robot Manipulators. London, U.K.: Springer Science & Business Media, 2001.
- [24] E. W. Weisstein, "Levenberg-marquardt method," 2000. [Online]. Available: https://mathworld.wolfram.com/
- [25] J. F. Epperson, An Introduction to Numerical Methods and Analysis. Hoboken, NJ, USA: John Wiley & Sons, Inc., 2021.
- [26] H. Wang, W. Chen, X. Yu, T. Deng, X. Wang, and R. Pfeifer, "Visual servo control of cable-driven soft robotic manipulator," in *Proc. IEEE/RSJ Int. Conf. Intell. Robots Syst.*, 2013, pp. 57–62.
- [27] T. Deng, H. Wang, W. Chen, X. Wang, and R. Pfeifer, "Development of a new cable-driven soft robot for cardiac ablation," in *Proc. IEEE Int. Conf. Robot. Biomimetics*, 2013, pp. 728–733.
- [28] P. Fairchild, N. Shepard, Y. Mei, and X. Tan, "Semi-physical modeling of soft pneumatic actuators with stiffness tuning," ASME Lett. Dyn. Syst. Control, vol. 3, 2023, Art. no. ALDSC-23-1050.